ELSEVIER

Materials Science and Engineering B91-92 (2002) 105–114

MATERIALS SCIENCE & ENGINEERING B

www.elsevier.com/locate/mseb

Near-field spectroscopy of a coupled wire-dot nanostructure grown on (311)A GaAs

Christoph Lienau [a,*], Francesca Intonti [a], Valentina Emiliani [a], Vincenzo Savona [b], Erich Runge [b], Roland Zimmermann [b]

[a] *Max-Born-Institut für Nichtlineare Optik und Kurzzeitspektroskopie, Max-Born-Str. 2A, D-12489 Berlin, Germany*
[b] *Institut für Physik, Humboldt Universität zu Berlin, Hausvogteiplatz 5-7, D-10117 Berlin, Germany*

Abstract

We discuss a detailed near-field spectroscopic study of the nanoscopic optical properties of a novel coupled wire-dot nanostructure grown on (311)A GaAs substrates. Photoluminescence spectra recorded with 150 nm spatial and 100 μeV spectral resolution permit mapping of two-dimensional variations of the lateral confinement potential and give direct information about growth dynamics. The absence of potential energy barriers between wire and dot makes these dots interesting optical markers for exciton diffusion via quantum well and wire states. The experiments indictate that exciton localization limits both the quasi-two and quasi-one-dimensional mobilities at low temperatures. The statistical parameters of the disorder potential underlying exciton localization, namely its correlation length and disorder amplitude are extracted by means of a novel statistical analysis of the two-energy autocorrelation function of ensembles of near-field PL spectra.

Keywords: Quantum wires; Quantum dots; Near-field optics; Luminescence spectroscopy

1. Introduction

In the last few years, the electronic and optical properties of two- and three-dimensionally quantum confined systems, i.e. quantum wires and dots, have been a central topic in solid state physics research. Semiconductor nanostructures represent important model systems for studying the fundamental physical properties of confined carriers and their excitations. In addition, potential device applications of such nanostructures in advanced optoelectronic devices are under investigation.

Optical spectroscopy is a most powerful tool for providing detailed information about the fundamental physical properties of semiconductor nanostructures. Yet, size and/or shape fluctuations in ensembles of such nanostructures give rise to rather strong fluctuations of the quantized electronic levels and the corresponding optical transition energies. This leads in general to a pronounced inhomogeneous broadening of optical spectra when probed with conventional far-field techniques. Recent progress in optical microprobing, using, e.g. near-field optical microsocopy (NSOM) has allowed to address single nanostructures and to study their electronic properties. Both single quantum wires [1–5] and quantum dots [6–10] have been investigated in steady state-experiments. The combination of NSOM with time-resolved techniques [11–14] has opened the possibility to image carrier dynamics in single nanostructures by performing space and time resolved experiments.

In this paper, we use this high spatial resolution technique to study the coupling mechanisms between different types of low-dimensional nanostructures, specifically between quasi-one-dimensional quantum wires linked to dot-like areas in a GaAs/AlGaAs wire-dot structure grown by molecular beam epitaxy on patterned GaAs(311)A substrate. The aim is to study exciton transport within quasi-one-dimensional nanostructures by using the dots as optical markers for exciton diffusion via quantum wire states. The experimental results demonstrate that exciton localization

* Corresponding author. Present address: Laboratorio Europeo di Spettroscopie non Lineari (LENS), I-50125 Firenze, Italy. Tel.: +49-30-6392-1476; fax: +49-30-6392-1489.
E-mail address: lienau@mbi-berlin.de (C. Lienau).

0921-5107/02/$ - see front matter
PII: S0921-5107(01)00953-9

within the quasi-one-dimensional disorder potential resulting from interface fluctuations limits the quasi-one-dimensional exciton transport at low temperatures. A new technique is demonstrated to quantitatively characterize the effective disorder potential that governs the excitonic transport, specifically its correlation length. This suggest a new way towards a systematic correlation of optical and transport properties of semiconductor nanostructures.

2. Samples

Quantum wires and coupled wire-dot nanostructures are fabricated by making use of the specific growth selectivity on patterned GaAs (311)A that differs qualitatively from that on low-index (100) and (111) substrates. Patterned growth on low-index substrates forms slow growing side facets due to the migration of adatoms away from the sidewalls to the mesa top and mesa bottom producing concave surface profiles in corners [15]. This is the basis for the formation of V-groove and ridge-type quantum wires and quantum dots. In contrast, in MBE growth of (Al,Ga)As on patterned GaAs (311)A substrates [01 − 1] oriented mesa stripes develop a slow growing side facet only on one side (left side of Fig. 1). On the opposite side which is in the sector towards the next (100) plane (right side of Fig. 1) a fast growing sidewall is formed. The surface profile of this very smooth fast growing sidewall is convex without any faceting and a well-defined corner at the mesa bottom is formed [16]. This new growth mechanism, which is unique for the [311]A substrate orientation [17], relies on the migration of adatoms from the mesa top and mesa bottom towards the sidewall. This is thus opposite in direction to that on patterned low-index substrates. Mesa stripes oriented along the perpendicular [− 233] direction develop slow growing side facets on both sides similar to patterned low-index substrates. The combination of this growth mechanism with appropriate lithographic patterning of the sample surface allows the controlled fabrication of novel nanostructures [18]. In particular, a quantum wire-dot structure has been realized by growth of a zig–zag pattern with sidewalls alternatingly misaligned by + or −30° from [01 − 1]. Fig. 2(a) shows a schematic top view of the structure. The sample consists of a nominally 3 nm thick GaAs QW layer clad between 50 nm $Al_{0.5}Ga_{0.5}As$ barriers. The upper barrier is covered by a 20-nm GaAs protective layer.

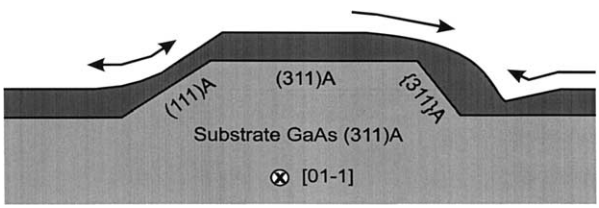

Fig. 1. Growth mechanism on patterned GaAs (311)A substrates with mesa stripes oriented along the [01 − 1] direction. The arrows indicate the preferential migration of Ga adatoms resulting in the formation of the fast growing sidewall.

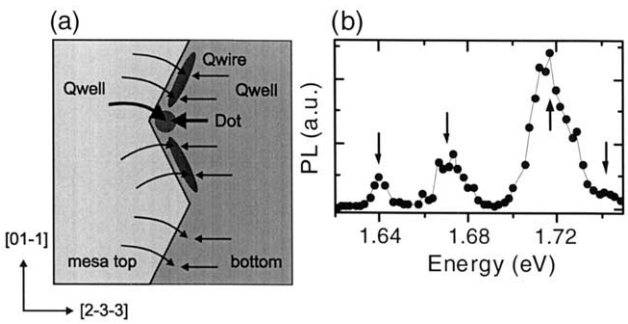

Fig. 2. (a) Schematic of the wire-dot nanostructure. (b) Far-field photoluminescence spectrum ($T = 10$ K) of the coupled wire-dot structure recorded with a spatial resolution of 3 μm by positioning the tip at the corner of the sidewall intersection.

3. Experimental

Spatially resolved near-field spectroscopic experiments were performed at temperatures between 10 and 300 K, with a home-built near field optical microscope [19]. For the optical characterization of the sample the microscope is used in the illumination/collection geometry: the excitation laser (photon energy 1.96 eV) is transmitted through the near-field fiber tip and the PL emitted from the sample is collected through the same fiber. High energy resolution images are recorded by acquiring PL spectra at each tip position with a $f = 50$ cm monochromator in conjunction with a liquid-nitrogen cooled back-illuminated charge coupled device (CCD) camera. We achieve a combined spatial and spectral resolution of 150 nm and 100 μeV, respectively. For the optical transport measurements, the microscope is used in the illumination geometry. A tunable narrow-band Ti:sapphire laser (bandwidth < 200 μeV) is coupled into the fiber tip for the excitation. The PL emission from the sample is collected in far-field through a conventional microscope objective, dispersed in a 0.25 m double monochromator with a spectral resolution of 1.2 meV and detected with a silicon avalanche photodiode. Spatially resolved images are recorded by scanning the probe tip over the sample.

Near-field fiber probes are made by chemically etching single mode optical fibers [20]. They are used in the illumination/collection mode without metal coating. When used in the illumination mode, the tips are coated with a 50–100 nm thick aluminium layer.

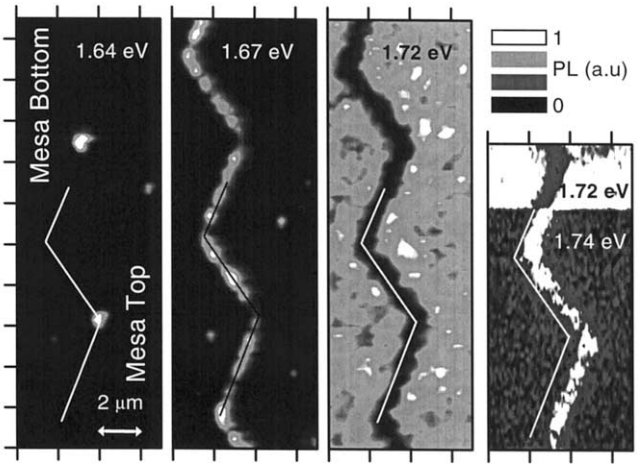

Fig. 3. Normalized near-field PL images recorded at the detection energies indicated in the figure and by arrows in Fig. 2(a). Excitation with He–Ne laser (1.96 eV).

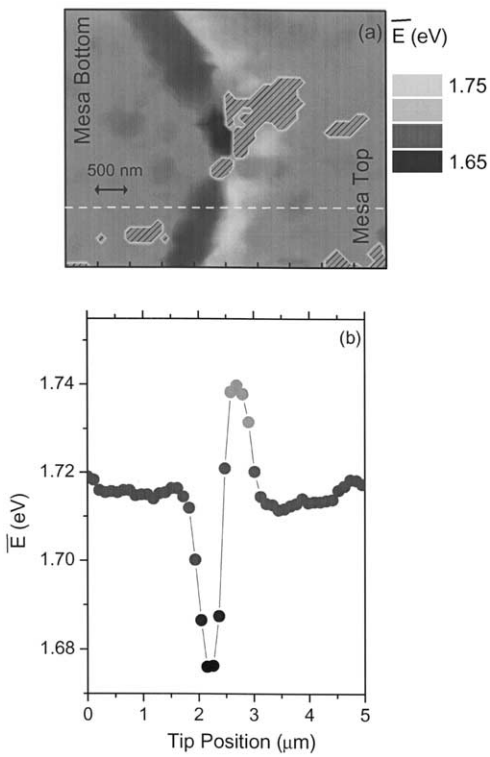

Fig. 4. Two-dimensional map of the average energy emission $\bar{E}(x,y)$. (b) Cross-section along the dashed line in (a). The patterned regions correspond to regions with a reduced luminescence yield that are not analyzed.

4. Local optical properties

An overview far field PL spectrum, Fig. 2(b), is recorded with the tip positioned near the corner of the intersection of two inclined sidewalls. Three major emission peaks at 1.64, 1.67 and 1.72 eV and a weak shoulder at 1.74 eV are visible. Their spatial origin is revealed by two-dimensional (2D) near-field images (Fig. 3). The low energy emission at 1.64 eV originates from dot-like regions at the corners of the two intersecting sidewalls that point toward the mesa top. QWR emission at 1.67 eV is observed along the zig–zag sidewalls, interrupted around the position where the first image reveals dot formation. The flat area QW emission PL at 1.72 eV extends on both mesa top and bottom. The emission at the weak shoulder, 1.74 eV, in the PL spectrum is located between QWR (dark area in the upper part of the image) and mesa top QW. It reflects an energy barrier separating these two regions [4,21].

The finding of such energy barriers is a clear indication that, during MBE growth, Ga adatom migration on these patterned (311)A substrates gives rise to a rather complex two-dimensional variation of the lateral quantum well thickness, and thus, of the lateral bandgap profile. Spatially and spectrally resolved near-field PL microscopy allows to directly and quantitatively map these lateral bandgap variations on a 100 nm scale. As shown below, such lateral band gap maps give direct insight into the growth mechanisms underlying the nanostructure formation. To this end, near-field PL spectra were recorded in illumination/collection geometry with high spectral resolution of 100 μeV in a 4×5 μm^2 scan range around the dot area with a pixel of 100 nm [22].

The result of such near-field experiments are three-dimensional sets of local emission intensities rather $I(x, y, E_{det})$, recorded as a function of lateral tip position (x, y) on the sample surface and of detection energy E_{det}. To analyze such complex three-dimensional sets of local emission intensities, $I(x, y, E_{det})$, average emission energies $\bar{E}(x,y)$ are extracted by performing weighted spectral averages of $I(x, y, E_{det})$ [22]. Using this information and a ratio of 1.5:1 for the conduction-to-valence-band offset energy in the 2D GaAs/AlGaAs structure, a 2D map of the GaAs layer thickness can be directly calculated in the effective-mass approximation with a finite-well model [21]. The extra confinement arising from the further reduction in dimensionality in the wire and dot regions is neglected in this simplified analysis, therefore at these positions the extracted values for the GaAs layer thickness are slightly underestimated by less than 0.1 nm.

The extracted $\bar{E}(x,y)$ map is depicted in Fig. 4(a). The plot highlights the pronounced local decrease $\bar{E}(x,y)$ along the QWR axis, and — even stronger — at the dot position. It also evidences the high energy barrier region surrounding the zig–zag pattern on the mesa top side. The curve in Fig. 4(b) is a representative cross-section through the 2D image (dashed line in Fig. 4(a)). On the mesa top $\bar{E}(x,y)$ increases with respect to the flat QW area by almost 24 meV over a length scale of about 500 nm as the QWR is approached. In contrast, on the mesa bottom the average QW emission

energy is constant and there is no evidence for barrier formation.

The resulting two-dimensional plot of the GaAs layer thickness is shown in Fig. 5. The flat QW area has an average thickness of 3.2 nm. As the QWR region is approached from the mesa top side, the average thickness goes down to 2.9 nm. This value corresponds to a decrease of about one monolayer with respect to the flat QW region. In the QWR region at the mesa sidewall the local thickness increases to about 3.8 nm, whereas the thickness in the dot-like region is estimated as 4.4 nm. No further thinning is present on the mesa bottom side.

The thinning of the QW in proximity of the sidewall is a consequence of Ga adatom migration towards the sidewall during the growth process. This adatom migration gives rise to the formation of a thicker GaAs region

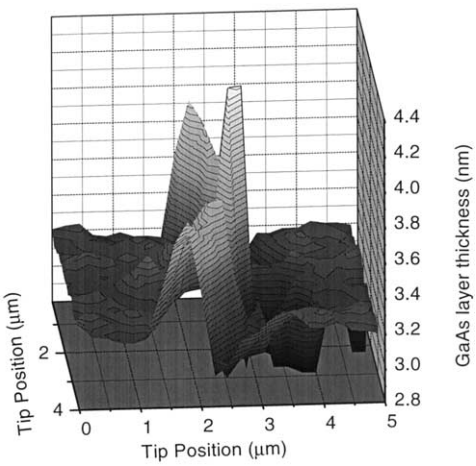

Fig. 5. Two-dimensional map of the GaAs layer thickness calculated from the average energy emission.

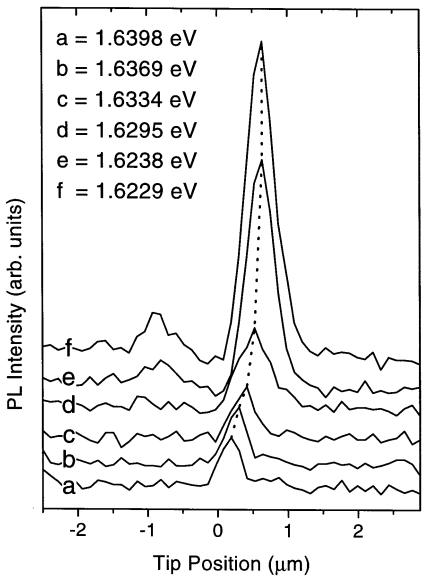

Fig. 6. Near-field PL profiles recorded perpendicular to the axis of the QWR at the detection energies indicated in the figure.

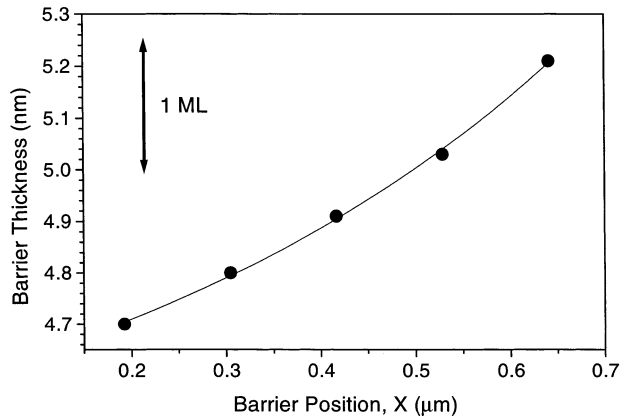

Fig. 7. Experimental variation of the barrier thickness as a function of the barrier position (closed circle) and fit assuming an exponential diffusion model (solid line). The arrow indicates the thickness of one GaAs monolayer, 2.83 nm.

at the edge (QWR formation) surrounded by thinner regions in the adjacent parts in the top and bottom areas. In this structure we observe a reduction of the QW thickness only on the mesa top side of the sidewall. This indicates that, during growth, migration of material occurs predominantly from the mesa top side and suggests that a strong asymmetry of the diffusion coefficient in the mesa top and bottom areas exists. Two-dimensional simulations of the surface pattern formation within a continuum drift-diffusion model confirm this point [22]. Such simulations show clearly that the nanostructure formation on these patterned substrates relies on the interplay between adatom surface diffusion driven by the spatial variation in particle density and by the local variation in surface chemical potential.

A closer inspection of the spatial evolution of the energy barrier separating wire and well allows to estimate the adatom diffusion length l_d from such local PL measurements. These experiments are performed on a reference QWR structure oriented along [01 − 1] based on a nominally 6 nm thick QW [4]. Near-field cross-sections perpendicular to the QWR axis (centered at 2.4 μm), Fig. 6, show a clear blue shift of the barrier emission as the QWR is approached: the closer the barrier position to the QWR the smaller the layer thickness. The barrier peak closest to the QWR corresponds to a 4.7 nm thick QW. The thickness difference with respect to that of the flat area QW decreases exponentially with increasing distance from the QWR, Fig. 7, and from this exponential decay an adatom diffusion length l_d of 550 nm is deduced. It is this adatom diffusion within a spatially inhomogeneous chemical potential created by lithographic patterning that governs nanostructure formation on (311)A GaAs substrates. Hence, intentional variations of the adatom diffusion length and/or the spatial variation of the chemical potential are important parameters for con-

trolling the lateral quantum confinement in these nanostructures [4].

A detailed knowledge of the local bandgap profile in the region around the dot area is of particular importance for the interpretation of quasi-one-dimensional transport studies, as local potential barriers separating QWR and dot are expected to strongly suppress carrier transport at low temperatures [21]. The average emission energy $\bar{E}(x,y)$ in a 2 μm × 2 μm region around the dot is plotted in Fig. 8(a) with a pixel of 50 nm. Within the experimental accuracy, no barriers are detectable at the wire-dot interface. This is evident from Fig. 8(b), showing a cross section of $\bar{E}$ along the wire axis as indicated by the white arrows in Fig. 8(a). This makes the sample suitable for optical transport studies using the dot as an optical marker for exciton diffusion via QW and/or QWRs states. Such studies will be presented in Section 5.

5. Near-field spectroscopy of quasi-one-dimensional exciton transport

To gain insight into the transport properties of the QWR, near-field PLE images of the dot area recorded.

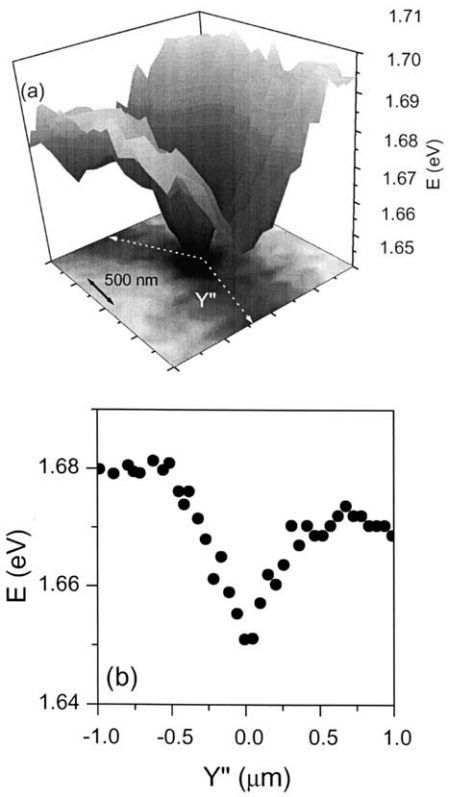

Fig. 8. (a) Detail of the average excitonic emission energy $\bar{E}(x,y)$ on a 2×2 μm^2 spot centered at the dot location. (b) Profile along the wire axis (dashed line in (a)).

The near-field microscope is now used in the collection geometry: the laser beam is coupled into the fiber and the PL signal is collected in far-field through a conventional microscope objective. The detection energy is fixed at the dot emission (1.64 eV) and the excitation energy is varied. Two-dimensional images of the dot emission with a 5.4 μm × 5.4 μm scan range are taken at three excitation energies, E_{ex}(QW), E_{ex}(QWR), E_{ex}(Dot), selected to create carriers resonantly to the lowest QW, QWR and dot transition.

The occurrence of dot luminescence after QW excitation involves carrier diffusion and trapping, i.e. a collection of carriers into the dot. It requires that both electrons and holes reach the dot region. Similar studies of quasi-two-dimensional transport using a QWR as an optical marker [11] have shown that the transport dynamics are dominated by excitonic transport at low temperatures of up to 100 K. As we are detecting time-integrated dot PL, we are insensitive to deviations from simple diffusive transport, expected to be of relevance on time scales shorter than the excitonic dephasing time of few picoseconds. In the absence of diffusion, the PL images recorded at the dot emission energy are expected to have approximately a circular shape centered at the dot position, with a diameter corresponding to convolution of spatial resolution and spatial extension of the dot PL. A finite diffusion length for resonant QW and QWR excitation leads to an increase in the image size, reflecting the 2D and/or 1D carrier transport.

Fig. 9(a,b) show the experimental data obtained at lattice temperatures of 10 and 80 K, respectively. At low temperatures (Fig. 9(a)), independent of the excitation energy, the images show the PL spatially located in a narrow region around the dot. At 80 K however a different situation appears (Fig. 9(b)). Depending on the excitation energy, the PL spatial distribution is strongly modified. It has a circular shape in the case of the QW excitation and reveals broad tails that extend exponentially into the wire region in the case of QWR excitation. Finally for excitation resonant with the dot we find the image of the dot broadened by the spatial resolution.

In Fig. 10(a,b) the spatial profiles of the PL at 80 K are extracted from the two-dimensional images reported in 9(b). The intensity of the PL is plotted (dots) versus the distance between the tip and the dot (X), when the tip is moved within the embedding QW (Fig. 10(a)) and along the QWR, respectively (Fig. 10(b)). PL spectra recorded for resonant QWR show that at this temperature the probability for thermally activated detrapping of QWR excitons into QW continuum states is small [4] allowing to separately analyze 1D and 2D excitonic transport. In both figures the PL intensity profile for E_{ex}(Dot) (dashed lines) show the broadening of the resolution. The experimental data are well described by

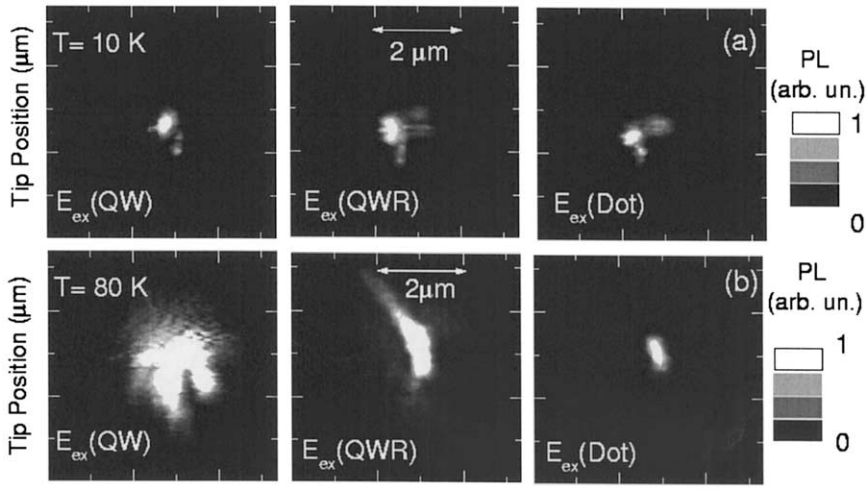

Fig. 9. Two dimensional NSOM images recorded with an etched coated tip at (a) 10 K and (b) 80 K. The excitation energies E_{ex}(QW), E_{ex}(QWR), E_{ex}(Dot) are selected in order to resonantly excite QW, QWR and Dot; the detection energy is tuned at the Dot PL peak.

assuming a simple, classical steady-state diffusion model with exitonic diffusion length L. Values of $L_{QW} = 650 \pm 100$ nm and $L_{QWR} = 600 \pm 100$ nm are derived for the QW and QWR diffusion length, respectively. From the low temperature data, where the spatial profile of the dot PL is limited by the spatial resolution, we extract for the diffusion lengths L_{QW} and L_{QWR} an upper limit of 120 nm.

From the observed diffusion lengths and the lifetime $\tau_{QW} = 1.3$ ns and $\tau_{QWR} = 1.5$ ns, measured in a similar structure [4], one can estimate the 2D and 1D diffusion coefficients $D_{QW} = L_{QW}^2/\tau$, $D_{QWR} = L_{QWR}^2/2\tau$ and the corresponding mobility μ_{QW} and μ_{QWR} via the Einstein relation $\mu = eD/k_BT$. We find diffusivities $D_{QW} < 0.1$ cm^2 s^{-1} and $D_{QWR} < 0.05$ cm^2 s^{-1} at 10 K, and $D_{QW} = 3$ cm^2 s^{-1} and $D_{QWR} = 1.2$ cm^2 s^{-1} at 80 K. The corresponding mobilities are $\mu_{QW} < 115$ cm^2 V^{-1} s^{-1} and $\mu_{QWR} < 60$ cm^2 V^{-1} s^{-1} at 10 K and $\mu_{QW} = 435$ cm^2 V^{-1} s^{-1} and $\mu_{QWR} = 175$ cm^2 V^{-1} s^{-1} at 80 K. The values of μ_{QW} are in good agreement with those reported for (100) GaAs quantum wells of similar thickness [23,24].

It is established that the 3D exciton mobility in GaAs can described by the inclusion of three mechanisms: scattering by ionized impurities, scattering by acoustic phonons via the deformation potential and polar-optical scattering [23]. In general, ionized impurity scattering limits the low temperature 3D mobility [23]. In 2D quantum wells alloy disorder in the quantum well barriers and nanoscale roughness of the quantum well interfaces gives rise to additional scattering mechanisms. Each of these scattering processes has a markedly different temperature dependence. Scattering by acoustic phonons and polar-optical scattering generally limit the mobility above 100 K [23,25].

At low temperatures and in thin QWs, interface-roughness scattering is clearly the dominant scattering mechanism. It gives rise to exciton localization in local potential minima [8,26] arising from microscopic fluctuations of the well width and limits the low temperature mobility. This is evidenced by a strong decrease of the low temperature exciton mobility with decreasing well width [23]. It is obvious that at low temperatures, interface roughness is also the mobility-limiting scattering mechanism in our samples. Both in the QW and QWR region interface-roughness scattering limits the 10 K exciton diffusion length to less than 120 nm, the resolution of our experiment. Hillmer et al. [27] proposed a simplified model relating the interface roughness limited low temperature mobility to the structural parameters describing the interface fluctuations, in this case the average diameter and height of homogeneous islands arising from monolayer height interface fluctuations. Comparing the measured mobilities of the 3.2 nm (311)A QW to this model one can conclude that the average island diameter should be larger than about 10

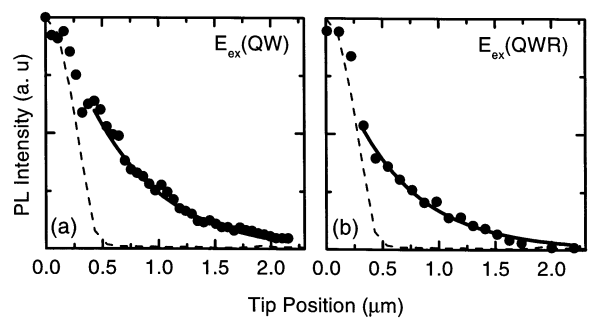

Fig. 10. Spatial profile of the dot luminescence at 80 K. (a) Excitation energy E_{ex}(QW), tip moved in the QW region. (b) Excitation energy E_{ex}(QWR), tip moved along the QWR axis. Dashed lines: spatial resolution.

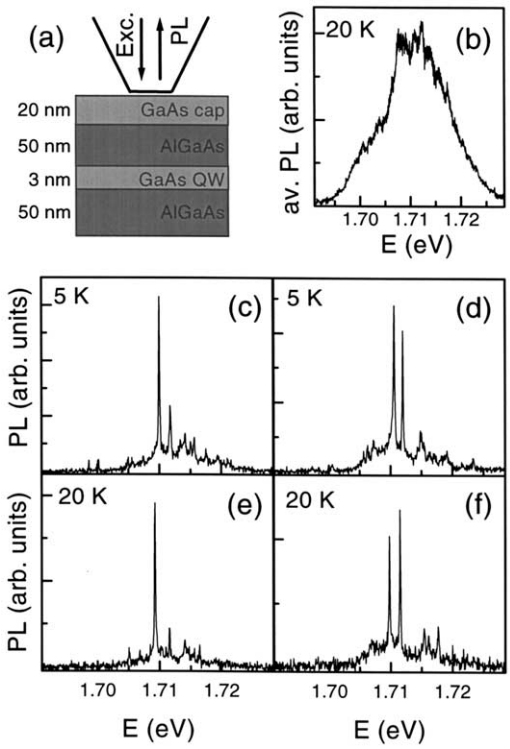

Fig. 11. (a) Schematic of the autocorrelation experiment. (b) Averaged PL far-field spectrum obtained by summing the 432 individual near-field spectra recorded in a $1.2 \times 3.6\ \mu m^2$ region. (c,d) Representative near-field spectra at two different spatial positions, recorded at 5 K. (e,f) Spectra at the same positions, recorded at 20 K.

nm. As will be seen in the next section this is in agreement with precise results obtained from a statistical analysis of the two-energy autocorrelation of near-field spectra.

With increasing sample temperature, the influence of interface roughness scattering decreases strongly, as evidenced by the pronounced increase in exciton diffusion length in both QW and QWR. Qualitatively, this increase in mobility reflects a thermally activated hopping-like transport of excitons that are localized in a random disorder potential. In the investigated structures, the thermal acitivation energies needed to observe finite diffusion lengths that are not limited by the spatial resolution of the experiments are similar to the quasi-one-dimensional subband quantization in our QWRs [4]. The subband splitting is about 7 meV in this sample as revealed from preliminary PLE experiments. Hence the quasi-one-dimensional quantization has only a weak influence on the exitonic mobility, in agreement with the experimental results. Hence, in both the quasi-two and quasi-one-dimensioanal areas of the coupled wire-dot nanostructure the low temperature excitonic mobility is most strongly affected by the quasi-zero-dimensional character of excitons localized in a random disorder potential arising from roughness at the interfaces.

6. Near-field autocorrelation spectroscopy

The results discussed in Section 5 highlight the important role of exciton localization in a disorder potential arising from nanoscale roughness at the quantum well and wire interfaces for the exciton transport dynamics. In order to correlate optical and transport properties of such disordered nanostructures, it is of key importance to have quantitative information about this disorder potential, specifically its correlation length and the nature of the localized exciton wavefunctions. Previous experiments with high spatial and spectral resolution have shown that smooth, inhomogeneously broadened PL lines observed in far-field spectroscopy break up into many narrow emission spikes from single localized excitons whose individual spectral widths are often determined by the experimental resolution or by the natural line width [8,28]. Yet, it has been proven difficult to directly relate the energy positions and/or widths of these individual lines to the microscopic parameters of the underlying disorder potential.

Here we demonstrate that a statistical analysis of the two-energy autocorrelation of near-field PL spectra gives precise information on both the correlation length of the disorder and the energy-dependent exiciton localization length.

We first demonstrate this novel experimental approach by analyzing near-field autocorrelation spectra recorded on the 3 nm (311)A QW area. Here, the sample is excited with light from a HeNe laser (1.96 eV) and near-field PL spectra are recorded in illumination/collection geometry (Fig. 11(a)) with a spatial and spectral resolution of 150 nm and 100 μeV, respectively. Sets of several hundred individual spectra are recorded by scanning a $1.2 \times 3.6\ \mu m^2$ area of the sample with steps of 100 nm. The spectrum that is obtained by averaging over the individual spectra shows a 15 meV inhomogeneously broadened emission band (Fig. 11(b)). In contrast to the averaged emission, the individual spectra break up into a set of spectrally sharp and intense emission lines [8,26,28]. Representative near-field spectra recorded at two different spatial positions at temperatures of 5 and 20 K are shown in Fig. 11(c–f). The spatial extension of the individual spikes is limited by our spatial resolution of 150 nm [26]. For excitation powers between 100 nW and 4 μW coupled into the fiber probe, the PL spectra show a linear intensity dependence and their shape is excitation intensity independent. The temperature and intensity independence of the PL spectra rules out biexcitonic transitions and makes contributions from charged excitons unlikely.

To explore the statistical parameters of the disorder potential we invoke the concept of level repulsion, a general feature of all quantum mechanical systems. If the wave functions of two eigenstates are spatially

overlapping, their eigenenergies can, in general, not be degenerate but split into two levels of different energy. Thus spatial correlations of excitonic wavefunctions should be reflected in energetic correlations of the corresponding levels [29]. Such energy correlations can be revealed by analyzing the two-energy autocorrelation function $R_c(\Delta E)$ of local spectra recorded with sufficiently high spatial resolutions. $R_c(\Delta E)$ is obtained by (i) calculating an energy autoconvolution of each individual spectrum, (ii) performing an ensemble average over these individual autoconvolutions and (iii) subtracting the autoconvolution of the spatially averaged spectrum, as described in detail in [29]. It is this subtraction procedure that removes contributions from pairs of spatially non-overlapping wavefunctions. As analyzed theoretically in Ref. [30], the resulting autocorrelation function is highly sensitive to the ratio σ/E_c related to the average amplitude of the disorder potential σ^2 and to $E_c = \hbar^2/2M\xi^2$. E_c is a natural energy unit for the exciton confinement in the center-of-mass approximation and determined by the exciton mass M and spatial correlation length ξ of the disorder potential. The disorder amplitude σ can be obtained from the inhomogoneously broadened far-field spectra or from the high energy part of autocorrelation, as discussed below. With the known exciton mass the autocorrelation function therefore provides a direct measure of ξ.

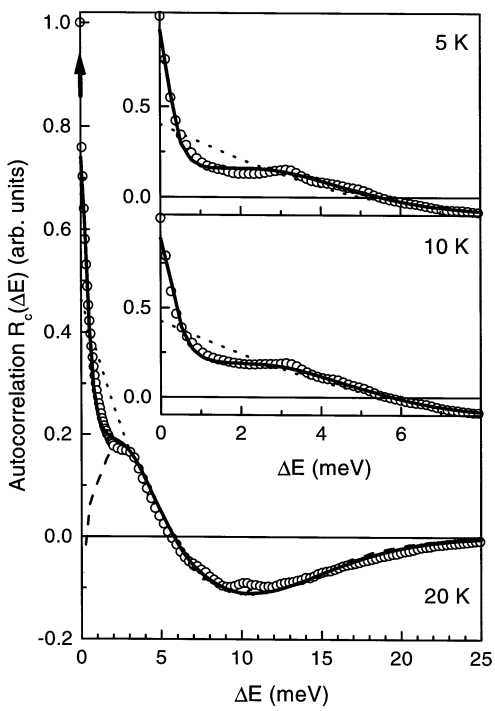

Fig. 12. The autocorrelation function $R_c(\Delta E)$ at $T = 20$ K is shown for the experimental data (circles), the Lorentz-convoluted numerical simulation (solid line), the classical limit (dotted line) and the raw numerical simulation (dashed). The arrow on the vertical axis denotes the δ-function part of the dashed curve. Insets: level repulsion region for $T = 5$ K and $T = 10$ K.

Fig. 12 shows the experimentally obtained QW autocorrelation function (open circles) for three different sample temperatures, 5, 10 and 20 K. The experimental curves at the three temperatures are similar and show three pronounced features: (i) the narrow spike around $\Delta E = 0$, due to the self-convolution of the individual, spectrally sharp localized exciton emission spikes. Its spectral width is defined by the homogeneous linewidth of the individual lines and the monochromator resolution. (ii) A pronounced shoulder for small ΔE values, around 2–3 meV, the signature of quantum mechanical level repulsion. (iii) At energies $\Delta E > 5$ meV, larger than the typical level repulsion correlation energies, the quantum mechanical contribution to the autocorrelation vanishes and the data follow the classical correlation function of the disorder potential. This qualitative discussion is strongly supported by comparing the experimental data to a detailed theoretical analysis, based on numerical simulations of the two-dimensional stationary Schroedinger equation in center-of-mass approximation [29]. The theoretically calculated autocorrelations (solid lines) are in excellent agreement with the experimental data and strikingly different from the classical autocorrelation (dotted line) which neglects level repulsion and is determined solely by the by the the energy correlation of the potential itself. At larger energies (region (iii)) both calculated and experimental $R_c(\Delta E)$ follow exactly this classical autocorrelation. The experimental autocorrelation remains essentially unchanged for excitation powers ranging from 100 nW to 4 μW and, as clearly seen in Fig. 12, also for temperatures between 5 and 20 K. This demonstrates that level repulsion repulsion of single excitons gives rise to the pronounced shoulder in $R_c(\Delta E)$. It also shows that this shoulder is a clear signature of the static disorder potential and, under these experimental conditions, only weakly affected by temperature-induced changes of the exciton distribution function and/or exciton-exciton interactions.

By comparing autocorrelations for different values of σ and ξ to the experimental data, we find that σ can be extracted with high accuracy by the large energy part of the classical autocorrelation. The potential correlation length ξ that is difficult to derive with other experimental methods, influences the energy position and amplitude of the level repulsion shoulder. This allows to determine the parameters of the investigated quantum well disorder potential the following values, $\sigma = (5.3 \pm 0.2)$ meV and $\xi = (17\ +8,\ -3)$ nm. It is straightforward to analyze the exciton COM localization length in such a disorder potential [31]. A detailed analysis indicates a strongly energy-dependent exciton localization length that varies between about 30 nm in the low energy part of the PL spectrum up to more than 100 nm in the high energy region of the spectrum.

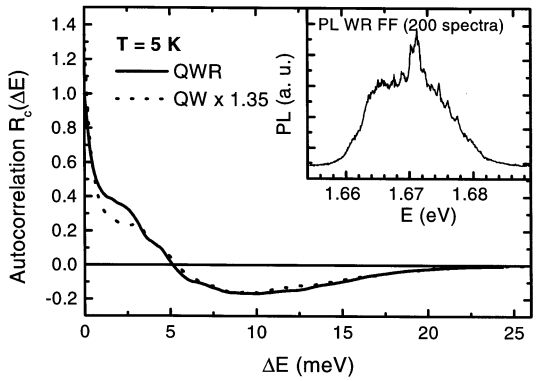

Fig. 13. Experimental autocorrelation function $R_c(\Delta E)$ at $T = 5$ K for the QWR (thick solid line) and QW regions (dotted line) of the sample. The inset shows the average quantum wire far-field PL spectrum.

Even for a given energy, the exciton localization length is found to be broadly distributed.

Similar ensembles of local near-field PL spectra were also recorded on the quantum wire region of the sample. These spectra are again dominated by spectrally sharp emission spikes from single localized excitons. Fig. 13 compares the resulting QWR autocorrelation (solid line) to that recorded on the QW region (dotted line). The QWR autocorrelation shows again a clear level repulsion shoulder, albeit less pronounced than on the QW part of the sample. Clearly, the large energy regions of $R_c(\Delta E)$, governed by the classical autocorrelation function, are very similar in both QW and QWR spectra. This shows that, within experimental error, the disorder amplitude σ is the same in both regions of the sample. The less pronounced level repulsion shoulder in the QWR spectra, indicates a slight increase in the correlation length of the effective QWR disorder potential as compared to the ξ_{QW}. This increase in the effective correlation length is likely to be linked to the quasi-one-dimensional confinement of the exciton wavefunctions rather than to a growth-induced variation in correlation length of the disorder potential in the two sample regions. A detailed analysis of this effect is currently underway.

In conclusion, near-field autocorrelation spectroscopy provides detailed new information on the spatial and energetic correlations of excitons in thin quantum wells. A combination of experimental near-field spectra and theoretical simulation give clear evidence for level repulsion in a disordered quantum well, allowing to quantify the correlation length of the disorder potential. This opens the way to a systematic correlation of optical and transport properties of semiconductor nanostructures and makes them important model system for studying the physics of wavefunction localization in disordered, random media.

Acknowledgements

This work was supported by the Deutsche Forschungsgemeinschaft (SFB296) and the European Union through the EFRE and SQID programs and Marie-Curie Fellowship ERB40001GT975127 and MCFI-1999-00728 for VE and VS, respectively. We gratefully acknowledge Richard Nötzel and Klaus Ploog for providing the coupled wire-dot samples and stimulating discussions.

References

[1] For a recent review see: Ch. Lienau, T. Elsaesser, in: K.T. Tseng (Ed.), Semiconductors and Semimetals, vol. 67, Academic Press, New York, 2001, p. 39.
[2] R.D. Grober, T.D. Harris, J.K. Trautman, E. Betzig, W. Wegscheider, L. Pfeiffer, K.W. West, Appl. Phys. Lett. 64 (1994) 1421.
[3] T.D. Harris, D. Gershoni, R.D. Grober, L. Pfeiffer, K. West, N. Chand, Appl. Phys. Lett. 68 (1996) 988.
[4] A. Richter, G. Behme, M. Süpitz, Ch. Lienau, T. Elsaesser, M. Ramsteiner, R. Nötzel, K.H. Ploog, Phys. Rev. Lett. 79 (1997) 2145.
[5] J. Hasen, L.N. Pfeiffer, A. Pinczuk, S. He, K.W. West, B.S. Dennis, Nature 390 (1997) 54.
[6] For a recent review see: A. Zrenner, J. Chem. Phys. 112 (2000) 7790.
[7] K. Brunner, U. Bockelmann, G. Abstreiter, M. Walther, G. Böhm, G. Tränkle, G. Weimann, Phys. Rev. Lett. 69 (1992) 3216.
[8] H.F. Hess, E. Betzig, T.D. Harris, L.N. Pfeiffer, K.W. West, Science 264 (1994) 1740.
[9] D. Gammon, E.S. Snow, D.S. Katzer, Appl. Phys. Lett. 67 (1995) 2391.
[10] Y. Toda, O. Moriwaki, M. Nishioka, Y. Arakawa, Phys. Rev. Lett. 82 (1999) 4114.
[11] A. Richter, M. Süptitz, D. Heinrich, Ch. Lienau, T. Esaesser, M. Ramsteiner, R. Nötzel, K.H. Ploog, Appl. Phys. Lett. 73 (1998) 2176.
[12] T. Guenther, V. Emiliani, F. Intonti, Ch. Lienau, T. Elsaesser, R. Notzel, K.H. Ploog, Appl. Phys. Lett. 75 (1999) 3500.
[13] M. Achermann, B.A. Nechay, U. Siegner, A. Harmann, D. Oberli, E. Kapon, U. Keller, Appl. Phys. Lett. 76 (2000) 2695.
[14] V. Emiliani, T. Guenther, C. Lienau, T. Elsaesser, R. Nötzel, K.H. Ploog, Phys. Rev. B 61 (2000) R10583.
[15] W.T. Tsang, A.Y. Cho, Appl. Phys. Lett. 30 (1997) 293.
[16] R. Nötzel, J. Menniger, M. Ramsteiner, A. Trampert, H.-P. Schönherr, K.-H. Ploog, Appl. Phys. Lett. 68 (1996) 1132.
[17] R. Nötzel, M. Ramsteiner, J. Menniger, A. Trampert, H.-P. Schönherr, L. Däweritz, K.-H. Ploog, Jpn. J. Appl. Phys. Part 2 35 (1996) L297.
[18] J. Fricke, R. Nötzel, U. Jahn, H.-P. Schönherr, M. Ramsteiner, K.H. Ploog, J. Appl. Phys. 86 (1999) 2896.
[19] G. Behme, A. Richter, M. Süptitz, Ch. Lienau, Rev. Sci. Instrum. 68 (1997) 3458.
[20] P. Lambelet, A. Sayah, M. Pfeffer, C. Philipona, F. Marquis-Weible, Appl. Opt. 37 (1998) 7289.
[21] Ch. Lienau, A. Richter, G. Behme, M. Süptitz, D. Heinrich, T. Elsaesser, M. Ramsteiner, R. Nötzel, K.H. Ploog, Phys. Rev B 58 (1998) 2045.
[22] V. Emiliani, F. Intonti, Ch. Lienau, T. Elsaesser, R. Nötzel, K.H. Ploog, Phys. Rev. B 64 (2001) 155316.

[23] H. Hillmer, A. Forchel, S. Hansmann, M. Morohashi, E. Lopez, H.P. Meier, K.H. Ploog, Phys. Rev. B 39 (1989) 10901.
[24] H. Hillmer, A. Forchel, R. Sauer, C.W. Tu, Phys. Rev. B 42 (1990) 3220.
[25] H. Hillmer, A. Forchel, C.W. Tu, Phys. Rev. B 45 (1992) 1240.
[26] F. Intonti, V. Emiliani, C. Lienau, T. Elsaesser, R. Nötzel, K.-H. Ploog, Phys. Rev. B 65 (2001) 075313.
[27] H. Hillmer, A. Forchel, C.W. Tu, J. Phys. Condens. Matter 5 (1993) 5563.
[28] D. Gammon, E.S. Snow, B.V. Shanabrook, D.S. Katzer, D. Park, Phys. Rev. Lett. 76 (1996) 3005.
[29] F. Intonti, V. Emiliani, Ch. Lienau, T. Elsaesser, V. Savona, E. Runge, R. Zimmermann, R. Nötzel, K.H. Ploog, Phys. Rev. Lett. 87 (2001) 076801 and references therein.
[30] V. Savona, R. Zimmermann, Phys. Rev. B 60 (1999) 4928.
[31] V. Savona, E. Runge, R. Zimmermann, F. Intonti, V. Emiliani, C. Lienau, T. Elsaesser, Phys. Stat. Sol. (b), in press.